buildings

MDPI

Article

Influence of Steel Fiber Content on the Fractal Evolution of Bending Cracks in Alkali-Activated Slag Concrete Beams

Xiaohui Yuan [1,2,*], Ziyu Cui [1,2] and Gege Chen [1,2]

[1] College of Architecture and Civil Engineering, Xinyang Normal University, Xinyang 464000, China; 13939099786@163.com (Z.C.); xy0104013@163.com (G.C.)
[2] Henan New Environmentally-Friendly Civil Engineering Materials Engineering Research Center, Xinyang Normal University, Xinyang 464000, China
* Correspondence: yxh@xynu.edu.cn

Abstract

This study systematically investigates the effect of steel fiber content on the fractal evolution characteristics of bending cracks in alkali-activated slag concrete (AASC) beams. A four-point bending test on simply supported beams, combined with digital image correlation (DIC) technology, was employed to quantitatively analyze the fractal dimension of crack propagation paths in AASC beams with steel fiber contents ranging from 0% to 1.4%, using the box-counting method. The relationship between fracture energy and fractal dimension was examined, along with the fractal control mechanisms of mid-span deflection, crack width, and the fractal evolution of fracture toughness parameters. The results revealed that as the steel fiber content increased, the crack fractal dimension decreased from 1.287 to 1.155, while the critical fracture energy of AASC beams increased by approximately 75%. Both mid-span deflection and maximum crack width were positively correlated with the crack fractal dimension, whereas the fractal dimension showed a negative correlation with critical cracking stress and fracture toughness and a positive correlation with the energy release rate. When the steel fiber content exceeded 1.2%, the performance gains began to diminish due to fiber agglomeration effects. Overall, the findings suggest that an optimal steel fiber content range of 1.0% to 1.2% provides the best crack control and mechanical performance, offering a theoretical basis for the design of AASC structures.

Keywords: steel fiber content; alkali-activated slag concrete; fractal dimension; crack evolution; fracture toughness

check for updates

Academic Editor: Rajai Zuheir Al-Rousan

Received: 11 June 2025
Revised: 6 July 2025
Accepted: 10 July 2025
Published: 11 July 2025

Citation: Yuan, X.; Cui, Z.; Chen, G. Influence of Steel Fiber Content on the Fractal Evolution of Bending Cracks in Alkali-Activated Slag Concrete Beams. *Buildings* **2025**, *15*, 2444. https://doi.org/10.3390/buildings15142444

Copyright: © 2025 by the authors. Licensee MDPI, Basel, Switzerland. This article is an open access article distributed under the terms and conditions of the Creative Commons Attribution (CC BY) license (https://creativecommons.org/licenses/by/4.0/).

1. Introduction

Alkali-activated slag concrete (AASC), a novel green and low-carbon building material, has gained significant attention in recent years. Zhang et al. [1] explored the bonding mechanisms of polyvinyl alcohol (PVA) fibers in alkali-activated slag/coal ash concrete through molecular dynamics simulations and experimental studies. Furthermore, research by Luga et al. [2] highlights the superior durability of AASC in seawater environments. After multiple wetting-drying cycles, its compressive and flexural strengths remain high, suggesting substantial potential for its application in coastal and marine engineering. However, challenges remain in the practical implementation of AASC in engineering projects. Salami et al. [3] highlighted that AASC faces issues such as rapid setting time and insufficient carbonation resistance. The rapid setting time may reduce the working time, thus increasing the difficulty of construction. In addition, poor carbonation resistance may lead

to the formation of microcracks on the concrete surface during carbonation, ultimately compromising its durability. Provis et al. [4] further demonstrated that the long-term durability of AASC is limited by shrinkage-induced microcracks. These microcracks not only weaken the concrete's strength but may also create pathways for the ingress of harmful substances, accelerating the material's deterioration. Additionally, Mundra et al. [5] identified that rebar corrosion significantly affects the durability of concrete. Corrosion of the reinforcement leads to spalling of the concrete cover, thereby reducing structural safety and service life. Although AASC offers excellent environmental benefits and specific durability, issues such as rapid setting time, carbonation resistance, shrinkage-induced microcracking, and rebar corrosion remain critical factors limiting its widespread application.

To address the mechanical performance limitations [6,7] of alkali-activated slag concrete (AASC), such as brittleness and susceptibility to cracking, researchers have introduced steel fiber reinforcement [8,9]. Xu et al. [10] conducted an in-depth study on the fracture characteristics of high-performance fiber-reinforced cement composites using acoustic emission (AE) and digital image correlation (DIC) techniques. The study found that steel fibers effectively control crack propagation, reduce the main crack width by 30–50%, and promote the formation of multiple secondary microcracks. However, there is currently a lack of systematic research on the influence of different fiber contents (0.5–2.0%) on the three-dimensional morphological characteristics and branching mechanisms of crack evolution. Specifically, there is an absence of mathematical models that quantitatively characterize the relationship between fiber content and crack network complexity. Rossi et al. [11] investigated the impact of single-hooked end and multi-hooked end steel fibers on the flexural and cracking resistance of alkali-activated slag concrete and ordinary Portland cement concrete. Three-point and four-point bending tests were conducted to evaluate the flexural strength and cracking resistance of the concrete, respectively. The results showed that the incorporation of steel fibers significantly enhanced both the flexural strength and cracking resistance of the concrete. Both single-hooked end and multi-hooked end steel fibers effectively improved the peak stress and strain of the concrete. Due to their unique geometry, multi-hooked end steel fibers can more effectively enhance the mechanical properties of concrete. Yuan et al. [12] investigated the flexural performance of concrete specimens reinforced with steel fibers of varying lengths, analyzing the effects of fiber type and content on peak load, fiber quantity in the section, load–displacement curves, section characteristics, and strain properties. The results showed that the addition of steel fibers significantly increased the peak load of the concrete specimens, with different fiber types exhibiting varying effects on the peak load. As the height of the specimens increased, the number of fibers in the section increased linearly. Furthermore, different types of steel fibers exhibited distinct characteristics in the residual stage of the load–displacement curves. The study showed that steel fibers effectively improved the fracture characteristics of the concrete, transforming its failure mode from brittle to a more ductile one. Hashmi et al. [13] studied the fractal characteristics of fatigue crack growth in complex geometries and proposed a new method to quantify the fatigue crack growth rate using fractal analysis. The study showed that the fractal characteristics of fatigue cracks effectively reflect the driving force at the crack tip, and the multifractal fatigue crack growth model can accurately predict the crack growth rate in complex geometries. The results were consistent with those predicted by the traditional Paris equation within a 99% confidence interval. Studies have shown that as the crack length increases, the fractal dimension also increases, reflecting the growing complexity and roughness of the crack surface. However, for the single steel fiber-reinforced AASC system, key scientific issues, such as the dynamic evolution of the fractal dimension with load and its relationship to macroscopic mechanical parameters,

remain underexplored. This limitation hinders the engineering application of fractal theory in this material system.

Meanwhile, with the development of deep learning methods [14,15] and numerical simulations [16–18], they have been widely applied to the analysis of various properties of concrete. For example, Li et al. [19,20] employed multiple algorithms to analyze bridge damage and bolt cracks, achieving goals such as real-time damage localization. In addition, the isogeometric boundary element method used by Chen et al. [21,22] has been successfully applied to electromagnetic scattering analysis and could potentially be extended to damage detection in beam structures in future work. The Bayesian neural network adopted by Lian et al. [23] also demonstrates considerable application potential in image analysis.

This study utilizes digital image correlation (DIC) technology combined with a four-point bending test to systematically investigate the impact of steel fiber volume fraction (0–1.4%) on the fractal characteristics of crack propagation in AASC beams. Fractal analysis is employed to quantify the fractal dimensions of the load–displacement curve at various stages, focusing on revealing the relationship between fracture energy and fractal dimension, the fractal control mechanism of mid-span deflection and crack width, and the fractal evolution patterns of fracture toughness parameters, such as critical cracking stress and energy release rate. The findings provide a fracture control method that combines theoretical insight with engineering practicality for AASC structural design.

2. Experiment

2.1. Materials

The apparent density of granulated blast furnace slag (GGBS) is 3.27 g/cm^3, with a specific surface area of 854.6 m^2/kg. A scanning electron microscope (SEM) image of GGBS is shown in Figure 1, illustrating its angular and irregular morphology. The apparent density of fly ash is 2.187 g/cm^3, and its SEM image is displayed in Figure 2, showing a smooth, spherical particle structure. Although gradation analysis was not conducted for the coarse aggregates, the particles were sieved to obtain the 5–20 mm fraction, as shown in Figure 3. The fineness analysis of fine aggregate was conducted according to the Chinese national standard GB/T 14684-2011 Sand for construction [24], as shown in Table 1. The fineness modulus of the fine aggregate was calculated to be 2.99 based on the standard sand fineness modulus formula. as depicted in Figure 4. The length of the corrugated steel fibers is 36 mm, with an equivalent diameter of 1.08 mm. The alkali activator is composed of a mixture of water glass, sodium hydroxide, and water, with the composition ratio presented in Table 2. The mix proportions for the alkali-activated slag concrete are provided in Table 3.

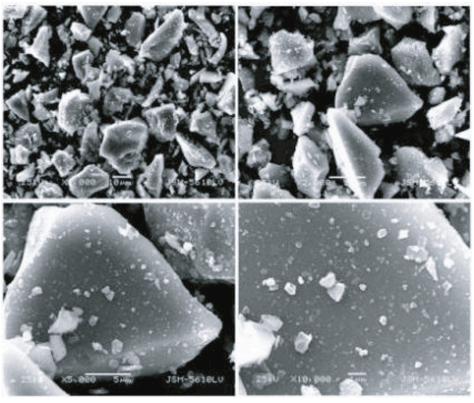


Figure 1. SEM image of slag.

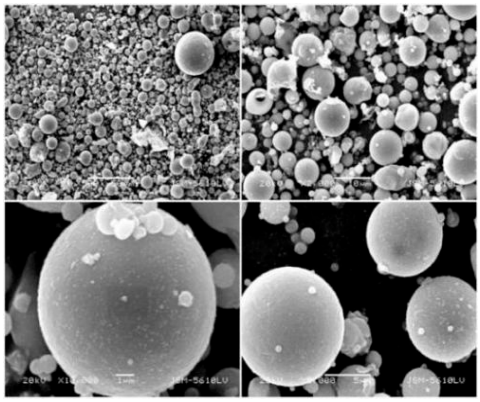


Figure 2. SEM image of fly ash.



Figure 3. Coarse aggregate.

Table 1. Particle size distribution of fine aggregate.

Particle Size/mm	4.75	2.36	1.18	0.6	0.3	0.15	Pan	Total Mass
mass/g	48.27	287.43	253.68	392.15	613.72	198.34	55.56	1857.15
mass percentage/%	2.60	15.47	13.66	21.11	33.04	10.68	2.99	99.99



Figure 4. Fine aggregates.

Table 2. Composition of the alkali activator solution for the AASC.

Water Glass Solution (%)	NaOH (%)	Water (%)	Moisture Content (%)
100	10.36	90.35	73.5

Table 3. Mix proportion design of steel fiber reinforced AASC.

Mix Proportion of the Concrete (kg/m^3)					Solution to Powder Ratio	Water to Solid Ratio	Steel Fiber Content
GGBS	Fly Ash	Fine Aggregate	Coarse Aggregate	Activator Solution			
280	120	615	1260	298.5	0.75	0.55	0.0%

2.2. Test Beam Design

In accordance with the "Technical Code for Fiber-Reinforced Concrete Structures." (CECS 38:2004) [24], a total of eight steel fiber reinforced alkali-activated slag concrete beams (SFRASC1 to SFRASC8) were designed, corresponding to steel fiber volume fractions of 0.0%, 0.5%, 0.9%, 1.0%, 1.1%, 1.2%, 1.3%, and 1.4%, respectively. According to the "Standard for Concrete Structure Test Methods" (GB/T 50152-2012) [25], the design parameters of the specimens are as follows: the beam cross-sectional dimensions are 120 mm × 200 mm, with a total length of 2000 mm and a concrete cover thickness of 25 mm; the aspect ratio of the cross-section should preferably be between 1.5 and 2.5; in this study, the aspect ratio is 1.67, which meets the requirement. The span-to-depth ratio should preferably range from 8 to 12; in this study, the ratio is 10, also compliant. No dimensional scaling was applied in this experiment. The reinforcement system consists of HRB400-grade tensile longitudinal bars 2C16 and frame bars 2C10, with HPB300-grade stirrups arranged as A8@100 mm. The details of the beam cross-section and reinforcement are shown in Figure 5, and the longitudinal reinforcement ratio ρ was calculated as follows:

$$\rho = \frac{A_s}{b \cdot h_0} \tag{1}$$

where A_s is the total area of longitudinal tensile reinforcement (mm^2), b is the width of the beam cross-section (mm), and $h_0 = h - a$, where h is the total section height, and α_s is the distance from the centroid of all longitudinal tensile reinforcement to the tension edge.

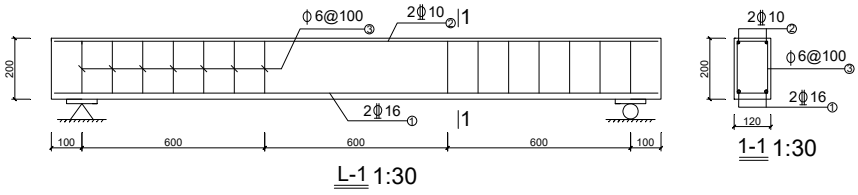


Figure 5. Dimensions and reinforcement illustration of the test beam (unit: mm).

2.3. Loading and Testing

According to the "Standard for Concrete Structure Test Methods" (GB/T 50152-2012) [25], a three-point concentrated loading method was employed, with fixed and roller hinge supports at both ends, respectively. To prevent localized stress concentration, steel shims were placed at the supports and loading points. The test load was applied to the specimen through a distribution beam. A schematic diagram of the loading device is shown in Figure 6.

A comprehensive monitoring scheme was implemented to quantify the deformation characteristics and crack development patterns of the test beams. The specifications of the measurement devices used in the experiment are as follows: the dial gauge has a reading accuracy of 0.01 mm; the strain gauges attached to the steel reinforcement offer high measurement precision, up to 0.1 με, while the strain gauges used on the concrete surface have an accuracy of 1 με.

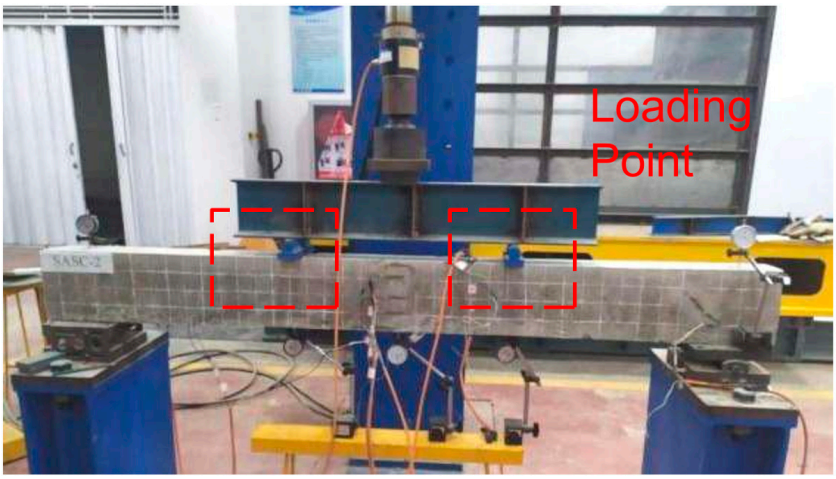


Figure 6. Loading device diagram.

Precision dial gauges were installed at the lower surface of the mid-span and at the upper surface of the support centers to monitor the vertical deformation data of the test beams. Five concrete surface strain gauges, spaced 45 mm apart, were uniformly arranged along the mid-span side surface of the beam to monitor the strain gradient distribution across the cross-section. Additionally, two steel surface strain gauges were positioned on the longitudinal reinforcement at the bottom of the mid-span to enable synchronous collection of strain data from the reinforcement. To accurately locate the initiation and propagation paths of cracks, a reference grid system with a 50 mm × 50 mm spacing was established on the side and bottom surfaces of the beam using the grid coordinate method. During the test, cracks were monitored in real-time through visual inspection. Once initial cracks were detected, marking lines were immediately drawn at the corresponding positions, and the load level and crack propagation length were recorded synchronously. The crack width was measured using an MG10085-1 type reading microscope, with a magnification of 100× and a minimum graduation value of 0.02 mm. A schematic diagram of the reading microscope is shown in Figure 7.



Figure 7. MG10085-1 reading microscope.

2.4. Analysis of Test Results

2.4.1. Load Result Analysis

The key load characteristics of the test beams at different steel fiber dosages are presented in Table 4. As shown in Table 4, with an increase in steel fiber content from 0.0% to 1.4%, the cracking load at the positive section, the cracking load at the inclined section, and the ultimate load increased by 60.1%, 49.3%, and 23.6%, respectively, demonstrating a significant positive correlation. This trend aligns with the findings in the literature [25,26],

confirming the beneficial effect of steel fibers on the cracking performance of alkali-activated slag concrete. It is noteworthy that when the steel fiber volume content reaches 1.0%, the cracking load at the positive section exhibits an anomalous fluctuation of approximately 8.7% compared to the 0.5% fiber content group. Observations of the failure surface revealed that fiber agglomeration was the direct cause of this fluctuation. When the steel fiber volume fraction in a localized region exceeds the critical value of approximately 1.2%, stress concentration points are formed, which in turn reduce the cracking threshold [27,28]. Furthermore, when the steel fiber content exceeds 1.0%, the probability of agglomeration increases significantly to 15–20%. The bridging effect of steel fibers has a dual impact on the structural load-bearing performance: on one hand, the ultimate load increases approximately linearly with fiber content, and a point of ductile failure transition is observed at a 1.2% fiber content. On the other hand, when the fiber content exceeds 1.0%, the efficiency of the incremental gain per unit of fiber decreases. This is primarily due to the reduced workability of the fresh concrete, which leads to a deterioration in molding density.

Table 4. Test load conditions of 8 test beams.

Number	Steel Fiber Content (%)	Cracking Load on the Cross-Section P_{cr} (kN)	Cracking Load of Inclined Section V_{cr} (kN)	Ultimate Load P_u (kN)
SFRASC1	0.0	15.8	45.2	89.4
SFRASC2	0.5	19.5	50.0	96.4
SFRASC3	0.9	22.1	55.2	100.2
SFRASC4	1.0	21.2	57.4	101.2
SFRASC5	1.1	22.8	60.7	103.8
SFRASC6	1.2	23.7	63.1	107.0
SFRASC7	1.3	24.4	65.7	108.0
SFRASC8	1.4	25.3	67.5	110.5

2.4.2. Deflection Results and Analysis

The mid-span deflection of the test beam was measured using five dial gauges. During loading, settlement occurred at both supports of the test beam; therefore, the measured mid-span deflection was adjusted by subtracting the average settlement of the supports. This is accurate only for the linear region in the load vs. mid-span deflection curves. Figure 8 presents the load-mid-span deflection curves for eight test beams. From Figure 8, it can be observed that, before cracking, the mid-span deflection of the test beam increased gradually in a linear fashion as the load increased. Although the steel fiber content varies among the test beams, the load-midspan deflection curves demonstrate substantial overlap during this phase. Throughout this stage, the beams remain within the elastic range. After cracking, the load-deflection curve displays its first inflection point, where the slope decreases, beam stiffness reduces, and the midspan deflection rate accelerates. Under the same load, beams made of steel fiber-reinforced alkali-activated slag concrete exhibit smaller deflections, and as the steel fiber content increases, the mid-span deflection further decreases. This is only accurate in the linear region of the load versus mid-span deflection curve. After the yielding of the longitudinal reinforcement, the rate of load increase slowed, and the mid-span deflection increased significantly. Notably, the incorporation of steel fibers led to a more gradual decline in the load-mid-span deflection curve, indicating that steel fibers significantly improved the toughness of the alkali-activated slag concrete and the ductility of the beams.

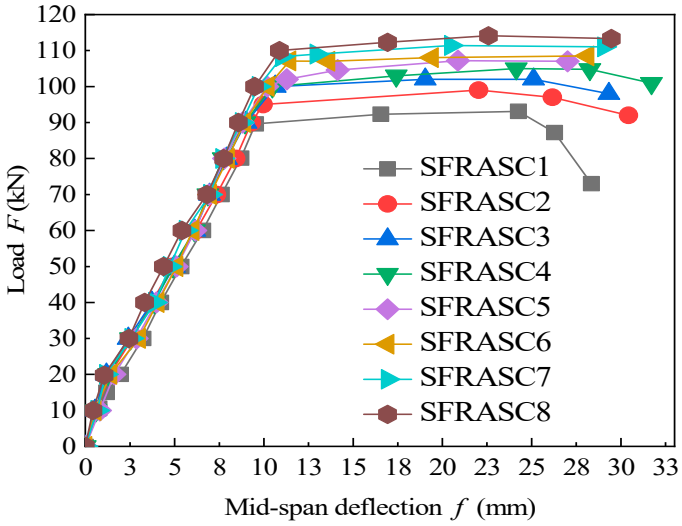


Figure 8. Load-deflection curves at midspan for eight test beams.

2.4.3. Crack Results and Analysis

Figure 9 shows the distribution and variation in the number of cracks in the test beams under different load levels. Overall, the specimens with steel fibers exhibited fewer cracks compared to those without steel fibers. From the figure, it can be observed that all eight test beams exhibited appropriate reinforcement failure, and their load-bearing process can be divided into three stages: elastic stage (load $\leq 0.3\ P_u$). In this stage, the influence of steel fibers on the beam's stiffness was relatively limited, but they significantly improved the cracking load. When the fiber content was greater than or equal to 0.8%, the position of the first crack shifted 15–20 mm from the mid-span toward the loading point, indicating that the steel fibers altered the distribution pattern of internal stresses within the beam; crack propagation stage ($0.3\ P_u \leq$ load $\leq 0.8\ P_u$). When the steel fiber content reached 1.4%, the number of primary cracks decreased by approximately 10%. This result is highly consistent with the "fiber-crack space interlocking mechanism" revealed by Zhang et al. [26] through X-ray tomography, indicating that steel fibers can effectively suppress the further propagation of cracks; failure stage (load $> 0.8\ P_u$), in this stage, steel fibers effectively inhibit the through-cracking of the beam and reduce the spalling area on the concrete surface. The force-induced failure results of the SFRASC1 test beam are shown in Figure 10. Microstructural analysis by Rossi et al. [29] indicated that this performance enhancement is primarily attributed to the densification effect of hydration products at the interface between the fibers and the matrix.

Table 5 presents the crack width and distribution characteristics of the eight test beams subjected to an 80 kN load. It can be observed that, under identical loading conditions, the crack width of steel fiber-reinforced alkali-activated slag concrete beams is significantly smaller compared with that of beams without steel fibers. According to the standard GB 50010-2010 [30], the allowable maximum crack width is generally 0.4 mm. The test results in this study mostly meet this requirement. Moreover, within a certain range, increasing the steel fiber content further reduces the crack width, demonstrating that steel fibers play a crucial role in effectively inhibiting crack propagation. As the fiber content rises, this inhibitory effect becomes more evident.

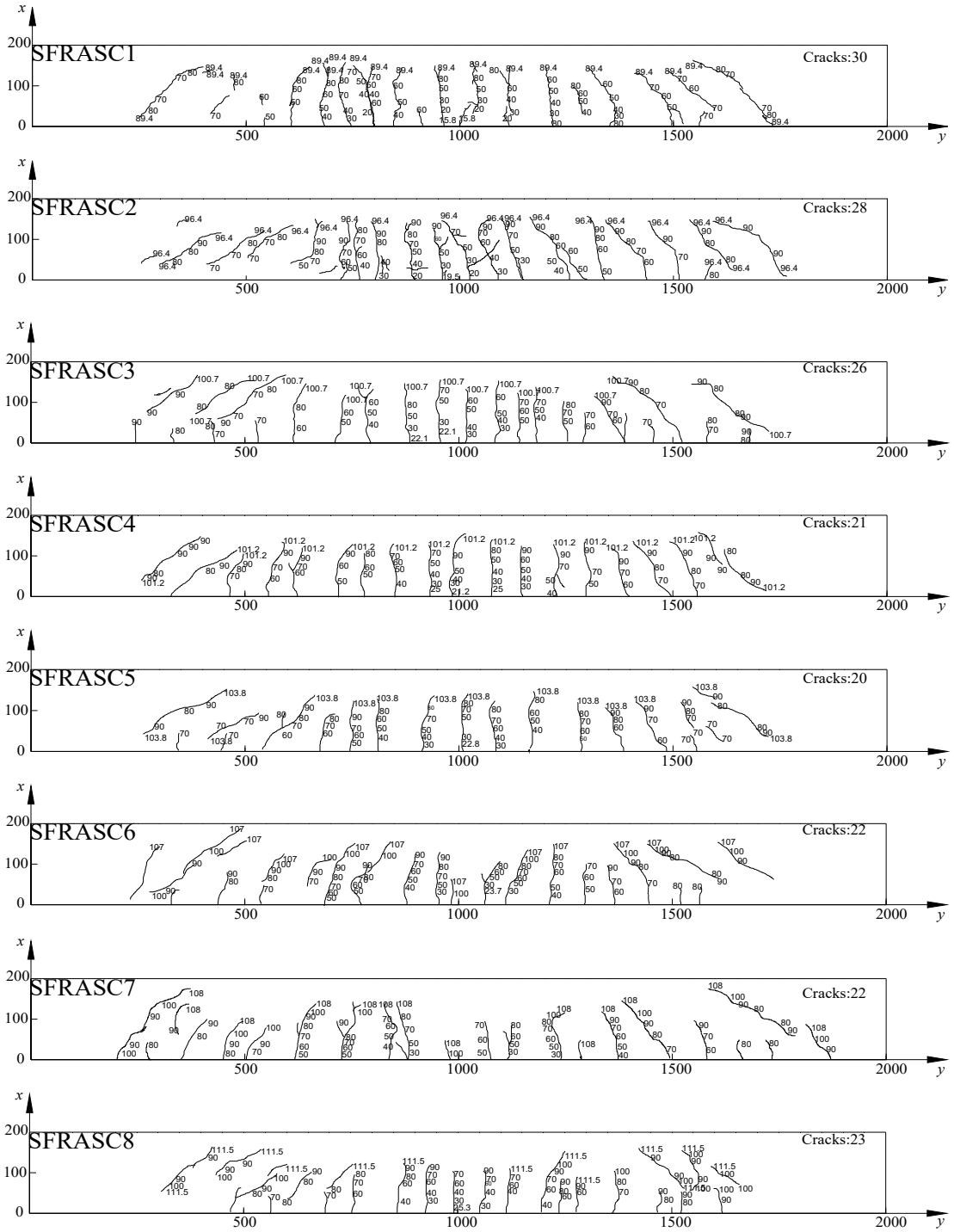


Figure 9. Crack propagation and distribution patterns of test beams across different groups under load.



Figure 10. Failure morphology of SFRASC1 test beam.

Table 5. Crack width and distribution characteristics of test beams subjected to an 80 kN load.

Number	Steel Fiber Content (%)	Width of Crack (mm)	Crack Distribution Characteristics
SFRASC1	0.0	0.50	Concentration and vertical development
SFRASC2	0.5	0.34	The main crack is clearly visible at mid-span, with only a few horizontal cracks observed.
SFRASC3	0.9	0.31	Cracks are interconnected, but their width increases at a slow rate.
SFRASC4	1.0	0.29	Diagonal cracks propagate in the bending-shear region.
SFRASC5	1.1	0.28	Crack intersections are observed, exhibiting complex propagation directions.
SFRASC6	1.2	0.26	The crack height is restricted, and the distribution is irregular.
SFRASC7	1.3	0.24	Cracks are tortuous, accompanied by numerous fine secondary cracks.
SFRASC8	1.4	0.23	Crack development remains limited, with relatively few secondary cracks.

3. Quantification and Analysis of Fractal Characteristics

3.1. Types of Fractal Dimensions

Fractal dimension is a fundamental quantitative measure in fractal geometry that characterizes the self-similarity and scale invariance of geometric structures using non-integer dimensional values. It provides a precise means of quantifying the complexity and disorder of these structures' topologies. The interpretation and calculation methods for fractal dimensions vary across different fields. The most commonly employed types of fractal dimensions are as follows.

Capacity Dimension [31]:

$$D_{cap} = \lim_{\varepsilon \to 0} \frac{\log N(\varepsilon)}{\log(1/\varepsilon)} \tag{2}$$

Here, D_{cap} represents the capacity dimension, and $N(\varepsilon)$ denotes the minimum number of boxes (or grids) having a side length of ε that are required to cover the fractal set.

Information Dimension [32]:

$$D_I = \lim_{\varepsilon \to 0} \frac{\langle \log P_i(\varepsilon) \rangle}{\log \varepsilon} \tag{3}$$

Here, D_I represents the information dimension; ε denotes the side length of the grid cells used to cover the fractal set; $P_i(\varepsilon)$ represents the probability of the fractal set within the i-th grid cell (such as mass ratio, density, etc.); $\log P_i$ refers to the logarithmic average weighted by probability, essentially reflecting the scaling behavior of Shannon entropy.

Correlation Dimension [33]:

$$D_C = \lim_{\varepsilon \to 0} \frac{\log C(\varepsilon)}{\log \varepsilon} \tag{4}$$

$$C(\varepsilon) = \lim_{N \to \infty} \frac{1}{N(N-1)} \sum_{i \neq j} \Theta\left(\varepsilon - \left\| x_i - x_j \right\|\right)$$

D_C represents the correlation dimension; $C(\varepsilon)$ denotes the probability that the distance between point pairs in the phase space is less than ε; let N denote the total number of data points in the set. For each of these N points, the corresponding spatial coordinates are represented as $(x_{i,}\ y_i)$, where i ranges from 0 to N. Θ is the Heaviside step function, defined as $\Theta(x) = 1$ for $x \geq 0$, and 0 otherwise; ε is the distance threshold.

Generalized Dimension [34]:

$$D_q = \lim_{\varepsilon \to 0} \frac{1}{q-1} \frac{\log \sum_{i=1}^{N(\varepsilon)} P_i(\varepsilon)^q}{\log \varepsilon} \tag{5}$$

D_q represents the generalized dimension; q is the order parameter, which adjusts the weight of different probability regions; $P_i(\varepsilon)$ is the probability of the fractal in the i-th grid at scale ε. When q takes values of 0, 1, and 2, the corresponding dimensions are the capacity dimension D_{cap}, information dimension D_I, and correlation dimension D_C.

Self-Similar Dimension [35]:

$$D_S = \lim_{\varepsilon \to 0} \frac{\log N}{\log(1/r)} \tag{6}$$

Here, D_S represents the self-similar dimension, and N is the number of substructures similar to the original structure, scaled by a factor of r.

A comparative analysis of the five types of fractal dimensions is presented in Table 6. The damage or surface morphology of the beam in this study is a non-strictly self-similar natural fractal, requiring a universal approach. This method directly quantifies the spatial complexity of the damaged area, utilizing the box-counting method for calculation.

Table 6. Comparative analysis of five fractal dimensions.

Type	Calculation Method	Applicable Scenarios	Advantages	Limitations
Capacity Dimension (D_{cap})	The box-counting method is used to compute the number of covering boxes, denoted as $N(\varepsilon)$	General fractals, such as cracks, surface roughness, or damage zones of beams	Strong versatility, straightforward calculation	Sensitive to image resolution; requires multi-scale fitting
Information Dimension (D_I)	Based on probability distribution P_i	Non-uniform fractals, such as mass distribution or energy dissipation	Quantifies distribution heterogeneity	Complex to calculate; requires large datasets
Correlation Dimension (D_C)	Correlation integral $C(\varepsilon)$ to analyze point pair distance distribution	Dynamical system attractors, time series, such as vibration signals	Suitable for analyzing chaotic systems	Requires phase space reconstruction; parameter sensitive
Generalized Dimension (D_q)	Multifractal spectrum	Multi-scale complex systems, such as turbulence or financial fluctuations	Provides a comprehensive characterization of multi-scale features	High computational cost; complex interpretation
Self-similarity Dimension (D_S)	Based on the number of subparts N and ratio r, derived from the generation rule	Strictly self-similar fractals, such as the Koch curve or Sierpinski carpet	Simple theoretical computation	Applicable only to ideal fractals, lacks universality

3.2. Fractal Expansion Model of Stress-Induced Cracks

In fracture mechanics, cracks [36] are classified into three basic types based on the applied stresses and fracture characteristics of the structure or component: Type I, Type II, and Type III [37]. A detailed illustration is provided in Figure 11. Type I cracks, known as opening-mode cracks, involve normal stress applied perpendicular to the crack surface. Type II cracks are shear-mode cracks, where shear stress is applied parallel to the crack surface and perpendicular to the crack tip line. Type III cracks, or tearing-mode cracks, involve shear stress applied parallel to both the crack surface and the crack tip line.

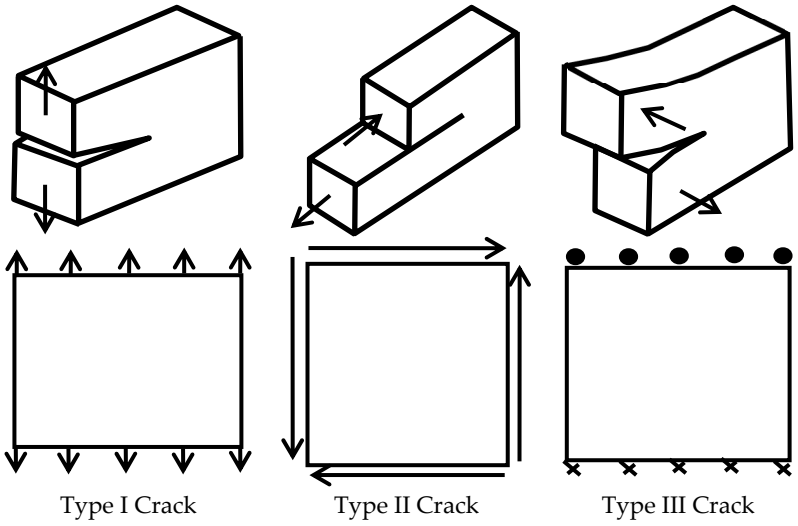


Figure 11. Basic types of concrete cracks.

This study, based on observations from four-point bending tests, found that crack propagation in steel fiber-reinforced alkali slag concrete beams predominantly exhibits Type I characteristics. The fractal evolution of these cracks can be characterized by critical stress, fracture toughness, and critical energy release rate. Wnuk and Yavari [38] extended Griffith's criterion [39] to fractal cracks and provided a modified expression for critical stress σ_c:

$$\sigma_c = \sqrt{\frac{2E\gamma_{\text{eff}}}{\pi\alpha^{2-D}}} \tag{7}$$

where E is the elastic modulus of the concrete material; γ_{eff} represents the effective surface energy, incorporating the influence of fractal geometry; and a is the characteristic length of the crack, with the projection length considered for fractal cracks.

$$\gamma_{eff} = \gamma_{matrix} + \rho_f J_b \tag{8}$$

γ_{matrix} is the fracture surface energy per unit area of the matrix material without fibers; ρ_f is the volume fraction of steel fibers; and J_b is the work of single fiber pullout.

Fracture toughness K_{IC} refers to the material's resistance to crack propagation. The relationship between fracture toughness, critical crack stress σ_c, and crack size a is described by Griffith's theory [39] as follows:

$$K_{IC} = \sigma_c \sqrt{\pi a} \cdot Y \tag{9}$$

Y is the dimensionless geometric factor, which depends on the crack shape and loading mode (typically, $Y \approx 1$ for a central crack).

Taking into account the fractal dimension D, the fracture toughness can be modified as follows [38]:

$$K_{IC}(D) = K_{IC} \cdot \left(\frac{a}{l}\right)^{\frac{D-1}{2}} \tag{10}$$

where l represents the microscopic scale, typically taken as 0.0001 m.

The critical energy release rate for crack propagation is an inherent property of the material, reflecting the concrete's ability to resist unstable crack growth. Under external loading, the energy release rate at the crack tip increases monotonically with the applied load. When this rate exceeds the critical value, the system enters an energy instability state, leading to dynamic crack propagation and ultimately causing brittle fracture of the concrete component. During Type I crack propagation in concrete, once the cracking stress reaches the tensile strength of the concrete, the fractal growth force reaches its maximum $G_{\max}$ [38].

$$G_{\max} = \frac{\mu\sigma_t^2}{2ED} a^{2-D} \delta^{D-1} \tag{11}$$

Here, μ represents the shape parameter of the crack zone, which is approximately taken as 2π.

4. Fractal Analysis of the Mechanical Properties of Steel Fiber Alkali-Activated Slag Concrete Beams

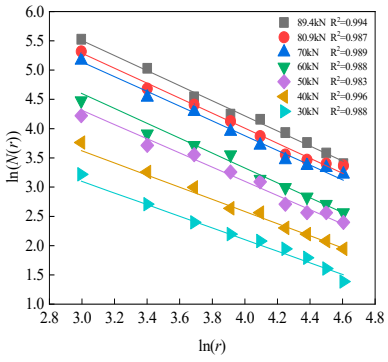
4.1. Calculation Results of the Crack Fractal Dimension

The box-counting Method is a classical technique used in fractal geometry to calculate the fractal dimension D. The procedure is as follows: first, the crack image is binarized, with pixel values set to one for the crack region and zero for the background, resulting in a clear binary image representing the crack distribution. Next, square grids of varying sizes r are applied to systematically cover the crack distribution map, and the minimum number of boxes $N(r)$ required to cover the crack area at each scale is counted. Then, a double logarithmic transformation is performed on the obtained r and $N(r)$ data, and the log–log relationship curve of $N(r)$ vs. r is plotted using MATLAB2018b software. If the data exhibit a strong linear correlation, the fractal dimension D is determined as the slope of the fitted line, which quantitatively describes the complexity and spatial expansion characteristics of the crack distribution.

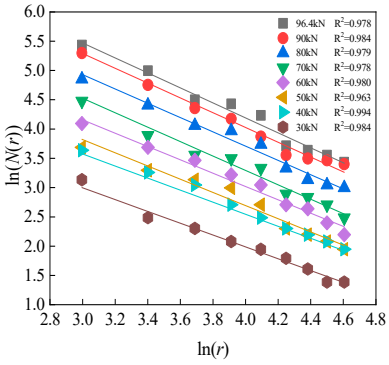
Wang et al. [40] highlighted in their research on the fractal characteristics of cracks in concrete members that, when applying the box-counting method, the selection of box sizes must meet specific conditions: the lower limit should not be smaller than the maximum particle size of the coarse aggregate, and the upper limit should not exceed the maximum crack spacing. If the selected range falls outside these limits, the calculation results may be biased, potentially yielding values lower than the topological dimension, which could lead to misjudgment of the fractal characteristics. Based on this conclusion, considering the concrete material characteristics used in this experiment (with coarse aggregate sizes ranging from 5 to 20 mm) and the observed crack distribution (with a maximum crack spacing of 100 mm), this study selected box sizes in increments of 20 mm, ranging from 20 mm to 100 mm. This selection range ensures an accurate representation of fractal characteristics while aligning with the material's microscopic structural features.

Figure 12 shows the log$N(r)$-log$r$ relationship curves for each test beam under failure conditions and various load levels. Figure 13 demonstrates that, during the staged loading process, the crack distribution of the steel fiber-reinforced slag concrete beams in each test group exhibits clear fractal scaling characteristics. Specifically, the log$N(r)$-log$r$ double logarithmic curve obtained using the box-counting method shows a high degree of linearity (correlation coefficient $R^2 > 0.95$) within the statistical scale range, from the maximum

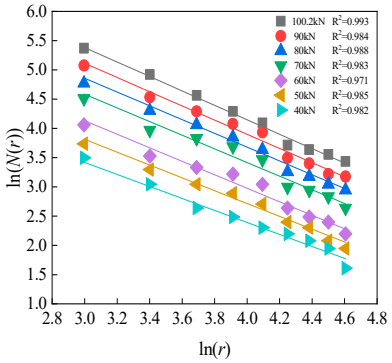
coarse aggregate particle size (20 mm) to the maximum crack spacing (100 mm). This scale invariance further supports the conclusion that the crack propagation path follows a statistically self-similar fractal structure.



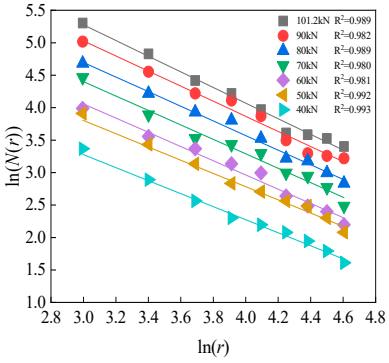
(**a**) ln$N(r)$-ln(r) curves of SFRASC1 under different loads



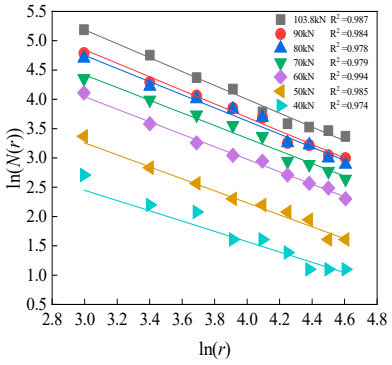
(**b**) ln$N(r)$-ln(r) curves of SFRASC2 under different loads



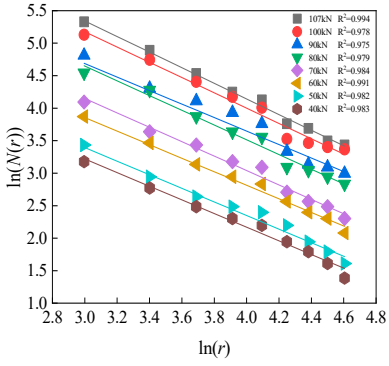
(**c**) ln$N(r)$-ln(r) curves of SFRASC3 under different loads



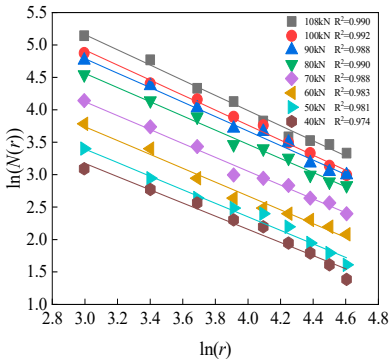
(**d**) ln$N(r)$-ln(r) curves of SFRASC4 under different loads



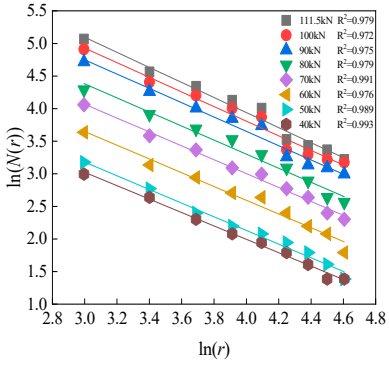
(**e**) ln$N(r)$-ln(r) curves of SFRASC5 under different loads



(**f**) ln$N(r)$-ln(r) curves of SFRASC6 under different loads



(**g**) ln$N(r)$-ln(r) curves of SFRASC7 under different loads



(**h**) ln$N(r)$-ln(r) curves of SFRASC8 under different loads

Figure 12. Relationship curves of crack propagation path and failure states of test beams under different loadings.



Figure 13. Failure modes of the eight steel fiber alkali slag concrete specimens (1 indicates agglomeration, 2 indicates no agglomeration).

Table 7 presents the test data for the fractal dimension *D* of cracks in each test beam under different load levels. Analyzing Table 7 reveals that as the load increases, the fractal dimension *D* of the test beams from SFRASC1 to SFRASC8 shows an upward trend. In the initial cracking stage, due to the low load, crack development is limited, resulting in a lower fractal dimension *D*. As the load gradually increases, the fractal dimension *D* remains between 1 and 2. For the same load, the fractal dimension *D* decreases as steel fiber content increases, indicating that the addition of steel fibers effectively suppresses the formation of microcracks and the propagation of macroscopic cracks in the concrete. This leads to a slower crack propagation rate and a more uniform crack distribution. In the failure stage, the fractal dimension *D* of the SFRASC1 test beam is 1.287, with a maximum load of 89.4 kN, while the fractal dimension *D* of the SFRASC8 test beam is 1.155, with a maximum load of 111.5 kN. Therefore, it can be concluded that as steel fiber content increases, the fractal dimension *D* decreases, the maximum load increases significantly, crack propagation is effectively delayed, and the fracture resistance of the test beam is enhanced.

Table 7. Fractal dimension *D* of cracks in test beams under different loadings.

Different Load Levels (kN)	Fractal Dimensions of Test Beams in Each Group							
	SFRASC1	**SFRASC2**	**SFRASC3**	**SFRASC4**	**SFRASC5**	**SFRASC6**	**SFRASC7**	**SFRASC8**
30	1.050	1.048						
40	1.116	1.075	1.066	1.034	1.046	1.057	1.030	1.028
50	1.147	1.116	1.092	1.074	1.061	1.067	1.053	1.047
60	1.176	1.156	1.119	1.099	1.075	1.077	1.067	1.055
70	1.217	1.174	1.140	1.119	1.096	1.100	1.077	1.065
80	1.247	1.203	1.159	1.134	1.116	1.124	1.097	1.079
90	1.287	1.225	1.199	1.173	1.139	1.154	1.120	1.105
100		1.280	1.245	1.215	1.184	1.183	1.148	1.121
110						1.211	1.170	1.155

4.2. Relationship Between Fracture Energy and Fractal Dimension

Considering the complexity of crack propagation paths in steel fiber-reinforced alkali slag concrete beams, fractal theory is used to analyze their crack propagation behavior under load. By establishing a quantitative relationship between the fractal dimension *D* and the energy dissipation per unit area of the crack band G_f, the influence of steel fiber content on the crack propagation path is further investigated. The fracture energy G_f is calculated based on the CEF-FIP Model Code 1990 specification [41].

$$G_f = G_{FO}(f_{cm}/f_{cmo})^{0.7} \tag{12}$$

In this study, G_{FO} represents the baseline fracture energy, which is determined based on the maximum aggregate diameter. Since the maximum aggregate diameter used in this experiment is 20 mm, G_{FO} is set to 0.037 N/m, f_{cmo} is 10 MPa, and f_{cm} corresponds to the

cubic compressive strength of the steel fiber alkali slag concrete material, as determined from experimental testing.

Table 8 presents the data for the critical fracture energy G_f and fractal dimension D of each experimental beam group. The analysis reveals an inverse correlation between the critical fracture energy and the fractal dimension of the crack propagation path in steel fiber alkali slag concrete beams. Specifically, as the fractal dimension decreases, the critical fracture energy increases. However, for the SFRASC5 beam with a steel fiber content of 1.1% and the SFRASC6 beam with 1.2% steel fiber content, an abnormal distribution of fracture energy was observed. It is hypothesized that insufficient mixing caused aggregation of a small portion of steel fibers, thereby reducing the strengthening effect of the fibers on the concrete. Here, we provide details regarding the aggregation of steel fibers. The mechanical properties of eight steel fiber alkali-activated slag concrete specimens (SFRASC1–SFRASC8) were evaluated using standard testing methods, and their failure results are presented in Figure 13.

Table 8. G_f and D values of test beams in each group.

Value	SFRASC1	SFRASC2	SFRASC3	SFRASC4	SFRASC5	SFRASC6	SFRASC7	SFRASC8
f_{cm} (N/mm^2)	30.5	38.5	46.6	47.5	53.8	55.1	59.2	67.6
G_f (N/m)	80.76	95.07	108.66	110.13	120.16	122.18	128.48	140.98
D	1.287	1.280	1.245	1.215	1.184	1.211	1.170	1.155

From the overall data trend, it is observed that as the steel fiber content increases, the fractal dimension of the experimental beams gradually decreases. This suggests that steel fibers, as an effective reinforcing material, can significantly reduce the formation of microcracks within the concrete structure or component, as well as the propagation of macrocracks. As a result, the energy required for crack fracture in the experimental beams increases, thereby enhancing the fracture resistance of the beams.

4.3. Relationship Between Mid-Span Deflection and Fractal Dimension

Mid-span deflection is a critical parameter for assessing the performance of structural components. In this experiment, the mid-span deflections of the SFRASC1 to SFRASC8 test beams were precisely measured under various loading conditions, while the corresponding fractal dimension D values of the crack propagation paths were simultaneously recorded. Using these data, the relationship between mid-span deflection and fractal dimension D for each test beam group was plotted. A fitting analysis was then performed, revealing the relationship curve between mid-span deflection and fractal dimension D for each beam group, with a correlation coefficient R^2 greater than 0.93, as shown in Figure 14.

As shown in Figure 14, a significant positive correlation is observed between the mid-span deflection of the experimental beams and the fractal dimension as the steel fiber content increases. As the mid-span deflection increases, the fractal dimension also rises, suggesting that the steel fibers effectively suppress crack propagation. The regression equation relating the mid-span deflection to the fractal dimension can be expressed as follows:

$$D = af^b \tag{13}$$

The values of a and b are shown in Table 9.

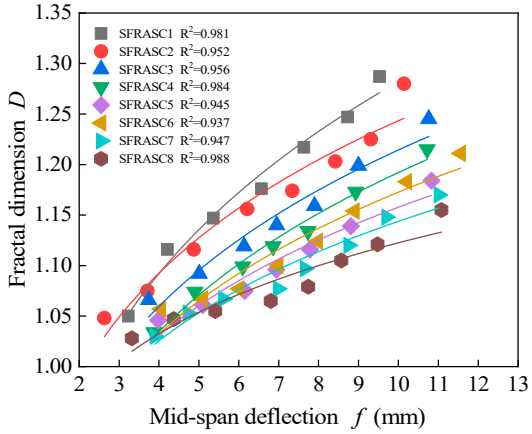


Figure 14. The relationship between the mid-span deflection and the fractal dimension for each group of test beams.

Table 9. Values of *a* and *b*.

Coefficient	SFRASC1	SFRASC2	SFRASC3	SFRASC4	SFRASC5	SFRASC6	SFRASC7	SFRASC8
a	0.00857	0.00868	0.00862	0.00835	0.00864	0.00851	0.00869	0.00910
b	0.175	0.141	0.149	0.155	0.127	0.139	0.119	0.091

4.4. Relationship Between Maximum Crack Width and Fractal Dimension

The fractal dimension *D* is a critical parameter for characterizing the morphology, distribution, and propagation characteristics of cracks in concrete, providing a quantitative reflection of the extent of damage. In concrete beams, crack formation and propagation are the primary indicators of damage, which significantly affect the structural load-bearing capacity. Fractal dimension *D* aids in assessing the complexity and irregularity of cracks by quantifying crack width. As existing cracks in concrete structures or components continue to propagate under load, new cracks form, and the crack widths progressively increase. Figure 15 illustrates the fitting curve between the maximum crack width at mid-span of the experimental beams and the fractal dimension *D* under various loading conditions, with a correlation coefficient R^2 exceeding 0.95.

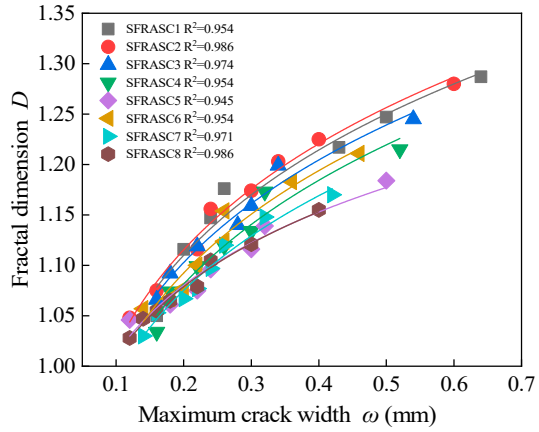


Figure 15. The relationship between the maximum crack width and fractal dimension for each group of test beams.

As shown in Figure 15, a significant positive correlation is observed between the maximum crack width and the fractal dimension across various load levels as the steel fiber content increases in the experimental beams. When the crack width reaches the

same level in different beam groups, those with higher steel fiber content exhibit smaller fractal dimensions, suggesting that steel fibers effectively suppress crack propagation. The regression relationship between the maximum crack width at mid-span and the fractal dimension can be expressed by the following equation:

$$D = g\omega^h \tag{14}$$

The values of g and h are shown in Table 10. As shown in Table 10, with the increase in steel fiber content, the rate at which the fractal dimension increases with the maximum crack width gradually decreases. When the steel fiber content reaches 1.4%, the values of g and h are 1.259 and 0.096, respectively, which represent decreases of 8.0% and 26.2% compared to alkali-activated slag concrete beams. This indicates that the rate of increase in the fractal dimension with the maximum crack width in the test beams gradually slows down. The analysis of the above experimental data shows that while the fractal dimension of the test beams increases with the maximum crack width, this growth trend gradually diminishes as the steel fiber content increases.

Table 10. Values of g and h.

Fit Coefficient	SFRASC1	SFRASC2	SFRASC3	SFRASC4	SFRASC5	SFRASC6	SFRASC7	SFRASC8
g	1.368	1.175	1.353	1.335	1.256	1.343	1.306	1.259
h	0.130	0.130	0.127	0.131	0.094	0.128	0.121	0.096

5. Relationship Between the Fracture Toughness and Fractal Dimension of Steel Fiber Alkali-Activated Slag Concrete Beam

For corrugated steel fibers, the pullout work J_b ranges from 1000 J/m^2 to 2000 J/m^2, with a value of 1500 J/m^2 used in this study. In the case of concrete without fibers, the unit area fracture surface energy γ_{matrix} of steel fiber alkali-activated slag concrete ranges from 40 J/m^2 to 100 J/m^2. According to the study in reference [42], the value of γ_{matrix} for steel fiber alkali-activated slag concrete with a 1.5 modulus water glass activator is 65 J/m^2. The crack characteristic length a is taken as the projected length of the cracks observed on the surface of the beam. According to the results shown in Figure 9, the values of a under the ultimate load are listed in Table 11. Finally, the calculation results for the critical cracking stress, fracture toughness, ultimate deflection and maximum energy release rate for the steel fiber alkali-activated slag concrete beams are presented in Table 11.

Table 11. Calculation results of fracture toughness for steel fiber alkali-activated slag concrete beams.

Volume Ratio of Steel Fiber ρ_f	Modulus of Elasticity (MPa)	Ultimate Deflection (mm)	Load (kN)	Characteristic Length of the Crack a (mm)	Fractal Dimension D	Critical Cracking Stress σ_c (Mpa)	Fracture Toughness K^f_{IC} (Mpa·m$^{1/2}$)	Maximum Energy Release Rate G^f_{max} (N/m)
0.0	26,000	9.53	89.40	158	1.287	5.396	10.939	52.163
0.005	26,000	10.14	96.40	144	1.255	7.560	12.851	124.026
0.009	27,000	10.76	100.20	155	1.245	8.735	14.991	182.764
0.01	28,000	10.72	101.20	154	1.230	8.903	14.403	205.856
0.011	28,000	10.83	103.80	136	1.225	9.542	14.044	223.677
0.012	29,000	11.56	107.00	154	1.211	9.220	13.911	248.916
0.013	30,000	11.01	108.00	143	1.170	8.985	11.168	300.481
0.014	31,000	11.08	110.50	123	1.155	9.645	10.406	333.258

The variation in the stiffness of steel fiber-reinforced alkali-activated slag concrete beams with different fiber contents is characterized by the change in ultimate stiffness, which is defined as the ratio of ultimate load to ultimate deflection. According to the results shown in Table 11, as the steel fiber content increases, the ultimate deflection gradually

increases. The ultimate stiffness increases from 9.38 kN/mm without fibers to 9.97 kN/mm at a fiber content of 1.4%, representing an increase of approximately 6.3%. This indicates that the incorporation of steel fibers can improve the stiffness of alkali-activated slag concrete beams, although the enhancement is limited. The fracture toughness shown in Table 11 increases as the steel fiber content rises from 0 to 0.009; however, when the fiber content exceeds 0.009, the fracture toughness overall shows a decreasing trend, indicating that the ductility exhibits a characteristic of first increasing and then decreasing.

5.1. The Relationship Between Critical Crack Stress and Fractal Dimension

As shown in Figure 16, the experimental results show that as the steel fiber volume fraction ρ_f increases from 0% to 1.4%, the critical cracking stress σ_c exhibits a nonlinear variation, initially increasing and then gradually stabilizing. When ρ_f was 1.1%, σ_c reached a peak value of 9.542 MPa, which is 76.8% higher than that of plain concrete. Simultaneously, the fractal dimension D of the cracks monotonically decreases from 1.287 to 1.155, representing a reduction of 10.3%. This change is attributed to the competitive mechanism between the bridging effect of the steel fibers and their distribution characteristics. When the fiber volume fraction ρ_f is less than or equal to 1.1%, the fibers are evenly distributed, forming a three-dimensional stress transfer network. The interface bonding strength and pullout work increase the energy consumed during crack propagation, which lowers the fractal dimension D and increases the critical cracking stress σ_c. However, when ρ_f exceeds 1.1%, the local agglomeration of fibers leads to stress concentration, which weakens the enhancement effect. This is reflected in the fluctuations of σ_c and the slower decrease in D. The strong negative correlation between σ_c and D indicates that the fractal dimension can serve as a quantitative indicator of crack suppression effectiveness. The threshold effect of ρ_f (critical value of 1.1%) highlights the role of the dispersion of the reinforcing phase in controlling the mechanical properties of the composite material, providing a theoretical basis for optimizing fiber content.

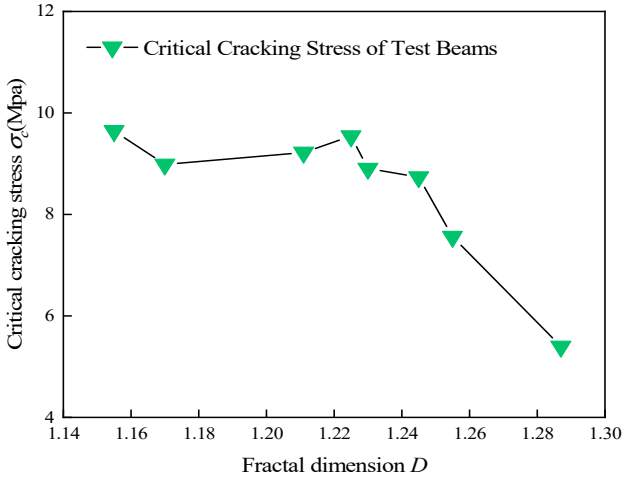


Figure 16. The relationship between the critical cracking stress of the test beam and the fractal dimension D.

5.2. The Relationship Between Fracture Toughness and Fractal Dimension

As shown in Figure 17, the test results demonstrate that the volume fraction of steel fibers ρ_f has a significant impact on both the fracture toughness K_{IC} and the fractal dimension D of crack evolution in concrete. As ρ_f increases from 0% to 1.4%, K_{IC} shows a non-monotonic trend, initially increasing and then decreasing, peaking at 14.991 MPa·m$^{1}/^{2}$ when ρ_f equals 0.9%, which is 37.0% higher than the value of plain concrete at 10.939 MPa·m$^{1}/^{2}$. However, once ρ_f exceeds 0.9%, K_{IC} gradually decreases,

dropping to 10.406 MPa·m$^{1/2}$ when ρ_f reaches 1.4%, a reduction of 31.5%. At the same time, the fractal dimension D monotonically decreases from 1.287 (at ρ_f = 0%) to 1.155 (at ρ_f = 1.4%), suggesting that the incorporation of steel fibers significantly modifies the complexity of crack propagation paths.

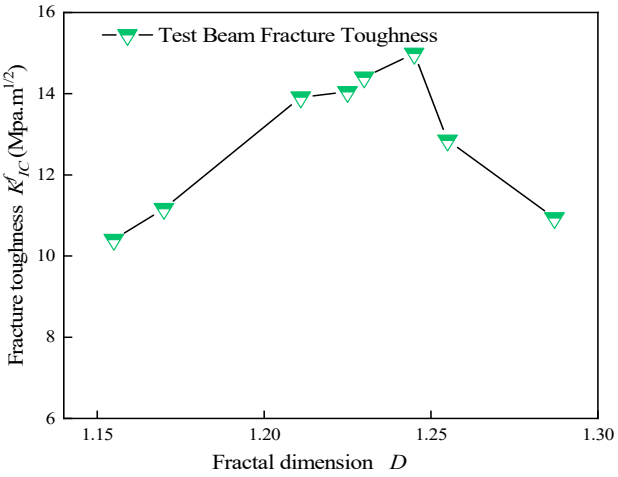


Figure 17. The relationship between fracture toughness and the fractal dimension D of the test beam.

From a micro-mechanical perspective, at lower fiber content levels ($\rho_f \leq 0.9\%$), steel fibers effectively delay crack propagation through bridging effects, thereby enhancing fracture toughness. During this stage, based on fiber spacing theory, the fiber distribution becomes more uniform, forming a continuous energy dissipation network that optimizes the fracture performance of the composite material. However, when ρ_f exceeds the critical threshold (approximately 0.9%), fiber agglomeration intensifies, leading to localized stress concentration and an increase in interface defects. This weakens the synergistic effect between the fibers and the matrix. Notably, when ρ_f > 1.2%, the fractal dimension D sharply decreases from 1.211 to 1.155, while K_{IC} significantly drops from 13.911 MPa·m$^{1/2}$ to 11.168 MPa·m$^{1/2}$, indicating that the uniformity of fiber distribution plays a critical role in fracture toughness. When the fiber content exceeds 1.2%, the deterioration of the microstructure leads to a decrease in the fracture toughness of the material.

5.3. The Relationship Between the Maximum Energy Release Rate and the Fractal Dimension

As shown in Figure 18, experimental studies have demonstrated that the fiber volume fraction ρ_f of steel fibers significantly impacts the fracture performance of concrete, exhibiting a typical dose–response relationship. As ρ_f increases from 0.0% to 1.4%, the maximum energy release rate grows exponentially, from 52.163 N/m to 333.258 N/m, an increase of 538.7%. In contrast, the fractal dimension D monotonically decreases from 1.287 to 1.155, a reduction of 10.3%. This apparent contradiction highlights the transition in the fracture mechanism of steel fiber-reinforced concrete: at lower fiber content levels ($\rho_f \leq 1.2\%$), steel fibers primarily enhance fracture resistance through discrete bridging effects. When ρ_f exceeds 1.2%, the fiber network density reaches a critical value, optimizing the crack propagation path (resulting in a more significant decrease in D), while the group bridging effect substantially improves energy dissipation efficiency (accelerating crack growth). This suggests the existence of a "crack path simplification-fracture resistance enhancement" synergistic mechanism in steel fiber-reinforced concrete.

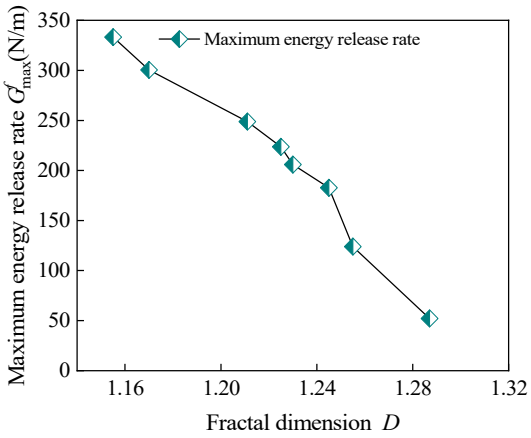


Figure 18. Relationship between the maximum energy release rate and fractal dimension D for the test beams.

6. Conclusions

The addition of steel fibers significantly influences the crack propagation behavior and overall structural performance of alkali-activated slag concrete. As the fiber content increases from 0% to 1.4%, the fractal dimension of cracks decreases from 1.287 to 1.155, indicating that steel fibers effectively reduce the complexity of crack propagation paths. In the range of 1.0% to 1.2% fiber content, the fiber bridging effect is most pronounced, simultaneously enhancing both the critical cracking stress and fracture toughness. However, when the fiber content exceeds 1.2%, the performance improvement begins to plateau due to the agglomeration of fibers.

A clear quantitative relationship exists between the fractal dimension and mechanical properties. The fractal dimension is negatively correlated with critical cracking stress and fracture toughness, while it shows a positive correlation with the energy release rate. The fractal model, established using the box-counting method, effectively characterizes the crack propagation behavior. Additionally, the modified Griffith criterion keeps the prediction error of critical stress within 5%, offering reliable theoretical support for engineering applications.

In practical engineering applications, maintaining fiber content within the optimal range of 1.0% to 1.2% is crucial to maximize structural benefits, including improved crack control, enhanced toughness, and better overall mechanical performance, while preserving good workability. Additionally, special care must be taken during mixing and casting to ensure uniform fiber dispersion and to avoid agglomeration, which can negatively impact structural integrity and long-term durability.

This study is based on a complete set of experiments, with a single static load test conducted for each mix proportion. In future work, we plan to increase the number of tests to obtain sufficient data for a comprehensive evaluation of the effects of steel fiber incorporation on structural performance and to apply statistical analysis methods to verify the significance of the results.

Author Contributions: Conceptualization, X.Y.; methodology, X.Y.; validation, X.Y.; investigation, Z.C. and G.C.; data curation, Z.C. and G.C.; writing—original draft preparation, Z.C. and G.C.; writing—review and editing, X.Y.; visualization, X.Y.; supervision, Z.C. All authors have read and agreed to the published version of the manuscript.

Funding: This work was supported by the 2025 Henan Provincial Science and Technology Research Project (Grant No. 252102230150) and the Postgraduate Education Reform and Quality Improvement Project of Henan Province (Grant No. YJS2025GZZ31).

Data Availability Statement: The general data are included in the article. Additional data are avail able on request.

Conflicts of Interest: The authors declare no conflicts of interest.

References

1. Zhang, S.; Duque-Redondo, E.; Kostiuchenko, A.; Dolado, J.S.; Ye, G. Molecular dynamics and experimental study on the adhesion mechanism of polyvinyl alcohol (PVA) fiber in alkali-activated slag/fly ash. *Cem. Concr. Res.* **2021**, *145*, 106452. [CrossRef]
2. Luga, E.; Mustafaraj, E.; Corradi, M.; Atiş, C.D. Alkali-Activated Binders as Sustainable Alternatives to Portland Cement and Their Resistance to Saline Water. *Materials* **2024**, *17*, 4408. [CrossRef]
3. Salami, B.A.; Ibrahim, M.; Algaifi, H.A.; Alimi, W.; Ewebajo, A.O. A review on the durability performance of alkali-activated binders subjected to chloride-bearing environment. *Constr. Build. Mater.* **2022**, *317*, 125947. [CrossRef]
4. Provis, J.L.; Palomo, A.; Shi, C. Advances in understanding alkali-activated materials. *Cem. Concr. Res.* **2015**, *78*, 110–125. [CrossRef]
5. Mundra, S.; Criado, M.; Bernal, S.A.; Provis, J.L. Chloride-induced corrosion of steel rebars in simulated pore solutions of alkali-activated concretes. *Cem. Concr. Res.* **2017**, *100*, 385–397. [CrossRef]
6. Zhang, W.; Liu, X.; Huang, Y.; Tong, M.-N. Reliability-based analysis of the flexural strength of concrete beams reinforced with hybrid BFRP and steel rebars. *Arch. Civ. Mech. Eng.* **2022**, *22*, 171. [CrossRef]
7. Zhang, W.; Yang, X.; Lin, J.; Lin, B.; Huang, Y. Experimental and numerical study on the torsional behavior of rectangular hollow reinforced concrete columns strengthened By CFRP. *Structures* **2024**, *70*, 107690. [CrossRef]
8. Gao, D.; Li, Z.; Ding, C.; Yu, Z. Uniaxial tensile stress-strain constitutive relationship of 3D/4D/5D steel fiber-reinforced concrete. *Constr. Build. Mater.* **2025**, *470*, 140539. [CrossRef]
9. Ghasemi, M.; Zhang, C.; Khorshidi, H.; Zhu, L.; Hsiao, P.-C. Seismic upgrading of existing RC frames with displacement-restraint cable bracing. *Eng. Struct.* **2023**, *282*, 115764. [CrossRef]
10. Xu, W.; Chen, Y.; Miao, H.; Zhang, L. An experimental study on fracture characteristics of high-performance fiber-reinforced cement composites through combined acoustic emission and digital image correlation. *J. Build. Eng.* **2025**, *103*, 112110. [CrossRef]
11. Rossi, L.; Zappitelli, M.P.; Patel, R.A.; Dehn, F. Flexural tensile behaviour of alkali-activated slag-based concrete and Portland cement-based concrete incorporating single and multiple hooked-end steel fibres. *J. Build. Eng.* **2024**, *98*, 111090. [CrossRef]
12. Yuan, P.; Ren, X.; Xie, Y. Experimental Study on the Flexural Properties of Steel-Fibre-Reinforced Concrete Specimens with Different Heights. *Sustainability* **2024**, *16*, 1900. [CrossRef]
13. Hashmi, M.H.; Koloor, S.S.R.; Abdul-Hamid, M.F.; Tamin, M.N. Fractal Analysis for Fatigue Crack Growth Rate Response of Engineering Structures with Complex Geometry. *Fractal Fract.* **2022**, *6*, 635. [CrossRef]
14. Niu, Y.; Wang, W.; Su, Y.; Jia, F.; Long, X. Plastic damage prediction of concrete under compression based on deep learning. *Acta Mech.* **2024**, *235*, 255–266. [CrossRef]
15. Chen, L.; Pei, Q.; Fei, Z.; Zhou, Z.; Hu, Z. Deep-neural-network-based framework for the accelerating uncertainty quantification of a structural–acoustic fully coupled system in a shallow sea. *Eng. Anal. Bound. Elem.* **2025**, *171*, 106112. [CrossRef]
16. Gong, B.; Li, H. A couple Voronoi-RBSM modeling strategy for RC structures. *Struct. Eng. Mech. Int. J.* **2024**, *91*, 239–250. [CrossRef]
17. Wang, K.; Cao, J.; Ye, J.; Qiu, Z.; Wang, X. Discrete element analysis of geosynthetic-reinforced pile-supported embankments. *Constr. Build. Mater.* **2024**, *449*, 138448. [CrossRef]
18. Chen, L.; Huo, R.; Lian, H.; Yu, B.; Zhang, M.; Natarajan, S.; Bordas, S.P. Uncertainty quantification of 3D acoustic shape sensitivities with generalized nth-order perturbation boundary element methods. *Comput. Methods Appl. Mech. Eng.* **2025**, *433*, 117464. [CrossRef]
19. Li, D.; Nie, J.H.; Wang, H.; Yu, T.; Kuang, K.S.C. Path planning and topology-aided acoustic emission damage localization in high-strength bolt connections of bridges. *Eng. Struct.* **2025**, *332*, 120103. [CrossRef]
20. Li, D.; Chen, Q.; Wang, H.; Shen, P.; Li, Z.; He, W. Deep learning-based acoustic emission data clustering for crack evaluation of welded joints in field bridges. *Autom. Constr.* **2024**, *165*, 105540. [CrossRef]
21. Chen, L.; Lian, H.; Liu, C.; Li, Y.; Natarajan, S. Sensitivity analysis of transverse electric polarized electromagnetic scattering with isogeometric boundary elements accelerated by a fast multipole method. *Appl. Math. Model.* **2025**, *141*, 115956. [CrossRef]
22. Chen, L.; Liu, C.; Lian, H.; Gu, W. Electromagnetic scattering sensitivity analysis for perfectly conducting objects in TM polarization with isogeometric BEM. *Eng. Anal. Bound. Elem.* **2025**, *172*, 106126. [CrossRef]
23. Lian, H.; Li, X.; Qu, Y.; Du, J.; Meng, Z.; Liu, J.; Chen, L. Bayesian uncertainty analysis for underwater 3D reconstruction with neural radiance fields. *Appl. Math. Model.* **2025**, *138*, 115806. [CrossRef]
24. *CECS 38:2004*; Technical Code for Fiber-Reinforced Concrete Structures. China Engineering Construction Standardization Association. China Planning Press: Beijing, China, 2004.

25. *GB/T 50152-2012*; Standard for Testing Methods of Concrete Structures. Ministry of Housing and Urban-Rural Development of the People's Republic of China. China Architecture and Building Press: Beijing, China, 2012; pp. 23–24.
26. Zhang, M.; Jing, J.; Zhang, S. Effect of steel fiber content on fatigue performance of high-strength concrete beams. *Sci. Rep.* **2025**, *15*, 11815. [CrossRef]
27. Chai, H.; Wu, H.; Zhang, Y.; Zhou, J.; Liu, D.; Yu, Y.; Liao, W. Research on the shear behavior of PBL connectors in steel fiber reinforced concrete composite beam. *Sci. Rep.* **2025**, *15*, 5824. [CrossRef]
28. Zheng, Y.; Lv, X.; Hu, S.; Zhuo, J.; Wan, C.; Liu, J. Mechanical properties and durability of steel fiber reinforced concrete: A review. *J. Build. Eng.* **2024**, *82*, 108025. [CrossRef]
29. Rossi, L.; Patel, R.A.; Dehn, F. New analytical models to predict the mechanical performance of steel fiber-reinforced alkali-activated concrete. *Struct. Concr.* **2025**, *26*, 236–247. [CrossRef]
30. *GB 50010-2010*; Code for Design of Concrete Structures. Ministry of Housing and Urban-Rural Development of the People's Republic of China. China Architecture and Building Press: Beijing, China, 2010; pp. 1–63.
31. Hentschel, H.G.E.; Procaccia, I. The infinite number of generalized dimensions of fractals and strange attractors. *Phys. D Nonlinear Phenom.* **1983**, *8*, 435–444. [CrossRef]
32. Mandelbrot, B.B.; Passoja, D.E.; Paullay, A.J. Fractal character of fracture surfaces of metals. *Nature* **1984**, *308*, 721–722. [CrossRef]
33. Grassberger, P.; Procaccia, I. Measuring the strangeness of strange attractors. *Phys. D Nonlinear Phenom.* **1983**, *9*, 189–208. [CrossRef]
34. Halsey, T.C.; Jensen, M.H.; Kadanoff, L.P.; Procaccia, I.; Shraiman, B.I. Fractal measures and their singularities: The characterization of strange sets. *Phys. Rev. A* **1986**, *33*, 1141. [CrossRef]
35. Song, C.; Havlin, S.; Makse, H.A. Self-similarity of complex networks. *Nature* **2005**, *433*, 392–395. [CrossRef] [PubMed]
36. Niu, Q.; Wang, J.; He, J.; Yuan, W.; Chang, J.; Wang, W.; Yuan, J.; Wang, Q.; Zheng, Y.; Shang, S. Evolution of pore structure, fracture morphology and permeability during CO_2+O_2 in-situ leaching process of fractured sandstone. *Energy* **2025**, *315*, 134348. [CrossRef]
37. Kaplan, M.F. Crack propagation and the fracture of concrete. *J. Proc.* **1961**, *58*, 591–610. [CrossRef]
38. Wnuk, M.P.; Yavari, A. On estimating stress intensity factors and modulus of cohesion for fractal cracks. *Eng. Fract. Mech.* **2003**, *70*, 1659–1674. [CrossRef]
39. Griffith, A.A., VI. The phenomena of rupture and flow in solids. *Philos. Trans. R. Soc. Lond. Ser. A Contain. Pap. Math. Phys. Character* **1921**, *221*, 163–198. [CrossRef]
40. Wang, T.; Yang, J. Fractal geometric analysis of crack state and its propagation in concrete structures. *J. Dalian Univ. Technol.* **1997**, *37*, 79–83.
41. Euro-International Concrete Committee. *CEB-FIP Model Code 1990*; Thomas Telford Ltd.: Lausanne, Switzerland, 1993.
42. Ding, Z.Y.; Zhou, J.H.; Su, Q.; Sun, H.; Zhang, Y.C.; Wang, Q. Influence of sodium silicate module on size effect of geopolymer recycled aggregate concrete. *Chin. J. Appl. Mech.* **2024**, *41*, 1394–1402. [CrossRef]

Disclaimer/Publisher's Note: The statements, opinions and data contained in all publications are solely those of the individual author(s) and contributor(s) and not of MDPI and/or the editor(s). MDPI and/or the editor(s) disclaim responsibility for any injury to people or property resulting from any ideas, methods, instructions or products referred to in the content.